Acta metall. Vol. 36, No. 1, pp. 81–93, 1988
Printed in Great Britain

0001-6160/88 $3.00 + 0.00
Pergamon Journals Ltd

A CONSTITUTIVE DESCRIPTION OF THE DEFORMATION OF COPPER BASED ON THE USE OF THE MECHANICAL THRESHOLD STRESS AS AN INTERNAL STATE VARIABLE

P. S. FOLLANSBEE and U. F. KOCKS
Materials Science and Technology Division, Los Alamos National Laboratory, Los Alamos, NM 87545, U.S.A.

(*Received* 31 *December* 1986; *in revised form* 21 *April* 1987)

Abstract—The axisymmetric deformation behavior of 0.9999 Cu is investigated at strain rates from 10^{-4} to $10^{4}\,s^{-1}$. The variations of the flow stress and of the mechanical threshold stress (the flow stress at 0 K), which is used as an internal state variable, with strain rate and strain are measured. The experimental results are analyzed using a model proposed by Kocks and Mecking: results at constant structure are described with thermal activation theory; structure evolution (strain and strain rate evolution of the mechanical threshold stress) is treated by the sum of dislocation generation and dynamic recovery processes. A significant result is that the athermal dislocation accumulation rate, or Stage II hardening rate, becomes a strong function of strain rate at strain rates exceeding $10^{3}\,s^{-1}$. This leads to the apparent increased strain rate sensitivity seen in a plot of flow stress at a given strain vs the logarithm of strain rate. An explanation is proposed for the strain rate dependence of this initial strain hardening rate based on the limiting dislocation velocity and average distance between obstacles.

Résumé—Nous étudions la déformation de symétrie axiale d'un cuivre 4N pour des vitesses de déformation allant de $10^{-4}\,s^{-1}$ à $10^{4}\,s^{-1}$. En fonction de la vitesse de déformation et de la déformation, nous mesurons les variations de la contrainte d'écoulement et de la contrainte seuil mécanique (la contrainte d'écoulement à OK) que l'on utilise comme variable d'état interne. Nous analysons les résultats expérimentaux à l'aide d'un modèle proposé par Kocks et Mecking: les résultats à structure constante sont décrits par une théorie d'activation thermique; l'évolution de la structure (évolution du seuil de contrainte mécanique en fonction de la déformation et de la vitesse de déformation) est traitée par la combinaison des mécanismes de création des dislocations et de restauration dynamique. Un résultat important est à soulingner: la vitesse d'accumulation athermique des dislocations, ou vitesse de consolidation du stade II, commence à dépendre fortement de la vitesse de déformation pour des vitesses de déformation supérieures à $10^{3}\,s^{-1}$. Ceci conduit à l'influence apparente accrue de la vitesse de déformation que l'on observe sur les courbes de la contrainte d'écoulement à déformation donnée en fonction du logarithme de la vitesse de déformation. Nous proposons une explication de l'influence de la vitesse de déformation sur la vitesse de consolidation initiale, explication fondée sur la vitesse limite des dislocations et la distance moyenne entre les obstacles.

Zusammenfassung—Das achsensymmetrische Verformungsverhalten von 0,9999 reinem Kupfer wurde für die Verformungsraten zwischen $10^{-4}\,s^{-1}$ und $10^{4}\,s^{-1}$ untersucht. Es werden die Fließspannung und die kritische mechanische Spannung (Fließspannung bei 0 K), die als eine Variable des inneren Zustandes verwendet wird, in Abhängigkeit von Verformungsrate und der Verformung gemessen. Die experimentellen Ergebnisse werden anhand des von Kocks und Mecking vorgeschlagenen Modelles ausgewertet. Die Ergebnisse für konstante Struktur werden mit der Theorie der thermischen Aktivierung beschrieben; die Entwicklung der Struktur (Entwicklung der kritischen mechanischen Spannung mit Dehnung und Dehnungsrate) wird mit der Summe von Versetzungserzeugung und dynamischen Erholungsprozessen behandelt. Ein wichtiges Ergebnis ist, daß die Rate der Versetzungsanhäufung, oder die Verfestigung im bereich II, oberhalb der Dehnungsrate von $10^{3}\,s^{-1}$ stark von der Dehnungsrate abhängig wird. Dieser Sachverhalt führt zu der scheinbar erhöhten Dehnratenempfindlichkeit, die sich in einem Diagramm der Fließspannung bei fester Dehnung gegen den Logaritnmus der Dehnungsrate bemerkbar macht. Für die Abhängigkeit dieser Anfangsverfestigung von der Dehnungsrate wird eine Erklärung vorgeschlagen, welche auf der begrenzenden Versetzungsgeschwindigkeit und dem mittleren Abstand zwischen den Hindernissen beruht.

1. INTRODUCTION

The deformation behavior of copper at high strain rates has been investigated in recent work by Follansbee [1] and Follansbee *et al.* [2]. This previous work has shown that the increased strain rate sensitivity (Fig. 1) typically observed at strain rates exceeding $\sim 10^{3}\,s^{-1}$ in copper and other metals of face-centered-cubic (f.c.c.) structure is an artefact of the practice of comparing flow stresses at constant strain, which is not a valid state parameter. When the comparison is instead made at constant structure (Fig. 2), where the mechanical threshold stress, or flow stress at 0 K, is used as the structure parameter, no increase in the strain rate sensitivity is observed in polycrystalline copper at strain rates as high as $10^{4}\,s^{-1}$. The constant-structure strain rate sensitivity continues to be controlled by the thermally activated interactions of dislocations with obstacles at these high strain rates: the previously postulated transition in rate controlling deformation mechanism from thermal activation control at low strain rates to

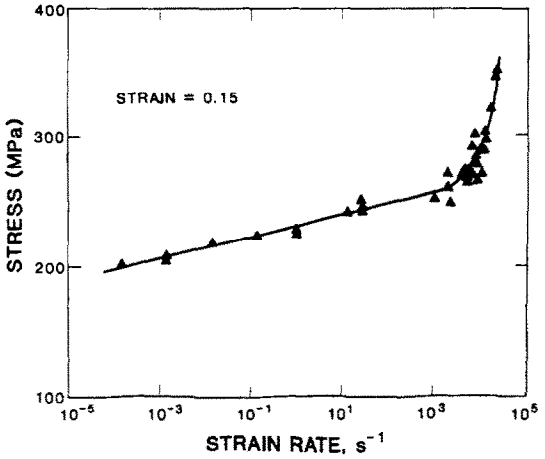

Fig. 1. Flow stress of annealed 0.9999 copper measured at a strain of $\epsilon = 0.15$ as a function of strain rate.

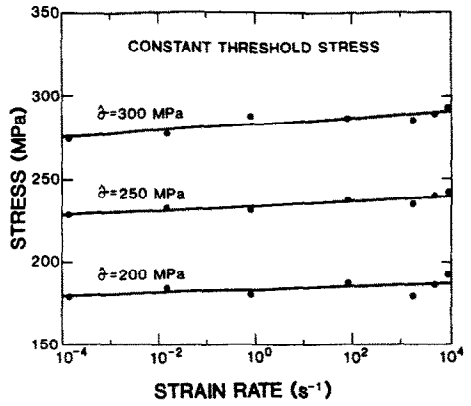

Fig. 2. Flow stress of annealed 0.9999 copper measured at a constant mechanical threshold stress as a function of strain rate [1, 2].

dislocation drag control at high strain rates [3, 4] does not occur at strain rates below $10^4\,s^{-1}$.

The observed change in the strain rate sensitivity at constant strain must then be due to the strain rate sensitivity of structure evolution. In the work of Follansbee *et al.*, this deduction was confirmed by measuring the mechanical threshold stress on dynamically deformed material and comparing this with the measured flow stress. A similar conclusion, however, was reached by previous investigators using flow stress measurements in strain rate change tests. Results in aluminum [5] and in copper [6–9] have indicated large strain or strain rate history effects. Measurements using the strain rate change test are usually limited to strain rates $< 10^3\,s^{-1}$. Because the strain rate sensitivity is found to increase at strain rates exceeding this, the intent of our previous work was to verify that history effects, and not a transition in glide mechanism, are responsible for the observed behavior; as described above, this indeed was the conclusion of these previous studies. The purpose of the present paper is to investigate these history effects more thoroughly. Specifically, our intent is to propose and test a physically based model that is used to describe the observed behavior in copper.

There have been numerous attempts to describe strain and strain rate history effects in f.c.c. metals at high strain rates. The presence of these history effects makes models that use strain as a state variable less plausible than those which incorporate some other internal state variable. Klepaczko [7] analyzed results of experiments in aluminum and copper and proposed a model based on the use of the dislocation density as the internal state variable and which incorporated the strain rate dependence of dislocation accumulation. More recently, Klepaczko and Chiem [10] reviewed the evidence for history dependence in f.c.c metals and proposed general relations for structural evolution, again based on dislocation accumulation and recovery mechanisms.

The Klepaczko–Chiem model has not been applied to data obtained at strain rates above $10^3\,s^{-1}$ where the constant-structure strain rate sensitivity increases. To describe the stress–strain behavior at these high strain rates, a common practice has been to use the experimentally observed linear relationship betwen strain rate and flow stress measured at constant strain [11, 12]

$$\sigma = \sigma_b + \beta\dot{\epsilon} \tag{1}$$

where σ_b and β are constants which can depend on strain. Although equation (1), when combined with an appropriate hardening law, can correctly represent monotonic stress–strain behavior at high strain rates, it is an unsatisfactory constitutive description for two reasons. First, it reintroduces strain as a state variable without allowing for the possibility of strain-path history effects. Second, the strain rate sensitivity expressed by equation (1) is

$$\frac{\partial \ln \sigma}{\partial \ln \dot{\epsilon}} = \frac{\beta\dot{\epsilon}}{\sigma_b + \beta\dot{\epsilon}} \tag{2}$$

which yields a value considerably higher (10–100 times) than the actual constant-structure strain rate sensitivity. Thus, there is a need for a single constitutive description which accounts for the high strain rate ($\dot{\epsilon} > 10^3\,s^{-1}$) as well as the low strain rate deformation behavior of f.c.c. metals.

In the present work the model of Kocks [13] and Mecking and Kocks [14] is applied and extended into the high strain rate regime. The model uses the mechanical threshold stress as an internal state variable and treats evolution of this variable using physically based and phenomenologically based expressions. (For a review of this model, see Estrin and Mecking [15].) The availability of mechanical threshold stress data measured in copper at strain rates as high as $10^4\,s^{-1}$ permits extension of this model into the regime where the strain rate sensitivity (determined at constant strain) is known to increase dramatically. This allows the proposal and testing of a single model based only on thermal activation controlled glide that describes experimental results

over a wide range of strain rates ($10^{-4}\,s^{-1} \leqslant \dot{\epsilon} \leqslant 10^{4}\,s^{-1}$). Although strain rate change tests are not used to generate data with which to fit the model, results of such tests are compared with predictions of the model. Finally, extrapolations of the model to temperatures and strain rates outside the regime where the model has been fit are investigated as a further test of the general validity of the proposed modeling procedure.

2. THEORY

We consider plastic deformation in a polycrystalline aggregate to occur by the accumulation and motion of dislocations and the rate controlling deformation mechanism to be the interactions of dislocations with "defects", i.e. grain boundaries, forest dislocations, solute atoms, etc. For pure f.c.c. metals the dominant short range obstacles are expected to be other dislocations (forest dislocations) whereas in solid–solution or dispersion strengthened alloys the contributions from several sources may have to be considered. In the present study we specify the flow stress σ as a function of a reference stress $\hat{\sigma}$ [14], the mechanical threshold stress, or flow stress at 0 K (in the absence of any drag or inertial influences). The mechanical threshold stress is separated into two components,

$$\hat{\sigma} = \hat{\sigma}_a + \hat{\sigma}_t, \tag{3}$$

where the component σ_a characterizes the rate independent interactions of dislocations with long-range barriers such as grain boundaries whereas the component σ_t characterizes the rate dependent interactions with short range obstacles. At finite temperature, thermal activation can lead to a lowering of the second component of the flow stress, while leaving the first unchanged. The relation between the flow stress and the mechanical threshold stress becomes

$$\sigma = \hat{\sigma}_a + \sigma_t = \hat{\sigma}_a + s(\dot{\epsilon}, T)\hat{\sigma}_t, \tag{4}$$

where the strain rate and temperature dependencies are included in the factor s†.

With equation (4) as a foundation for a model, there are two separate problems to consider. First, the form of the factor s in equation (1) must be specified. Second, evolution of the mechanical threshold stress must be described.

2.1. Thermal activation at constant structure

The factor s in equation (4) specifies the ratio between the applied stress and the mechanical threshold stress; its value is defined by the glide kinetics. This factor is <1 for thermally activated controlled glide because the contribution of thermal activation energy reduces the stress required to force a dislocation past an obstacle. If deformation is instead in the dislocation drag controlled regime, then an applied stress greater than the mechanical threshold stress is required for continued deformation. Although the exact form of the equation relating $\sigma(\hat{\sigma}, \dot{\epsilon}, T)$ in the transition regime between these two rate controlling deformation mechanisms has been derived by Regazzoni *et al.* [16], our previous results in copper indicate that at strain rates $< 10^{4}\,s^{-1}$ the rate controlling deformation mechanism is thermal activation and that the contribution of dislocation drag is negligible.

In the thermally activated glide regime the interaction kinetics for short range obstacles are described by an Arrhenius expression of the form

$$\dot{\epsilon} = \dot{\epsilon}_o \exp\left[\frac{\Delta G(\sigma_t/\hat{\sigma}_t)}{kT}\right], \tag{5}$$

where $\dot{\epsilon}_0$ is a constant and k is the Boltzmann constant. For the free energy ΔG we have chosen the phenomenological relation [16, 17]

$$\Delta G = g_o \mu b^3 \left[1 - \left(\frac{\sigma_t}{\hat{\sigma}_t}\right)^p\right]^q, \tag{6}$$

where g_o is a normalized activation energy, which is expected to remain constant providing the obstacle character does not vary, μ is the shear modulus, b is the magnitude of the Burgers vector, and p and q are constants that characterize the (statistically averaged) shape of the obstacle profile ($0 \leqslant p \leqslant 1$; $1 \leqslant q \leqslant 2$ [17]). Note that this form differs slightly from the form reported previously [1, 2] in the use of only the thermally activated part of the applied stress. Because at stresses larger than the yield stress $\hat{\sigma}_a$ is a small fraction of $\hat{\sigma}$, this difference is a minor one. Combining equations (6), (5), and (3) and rearranging the result gives

$$\sigma = \hat{\sigma}_a + (\hat{\sigma} - \hat{\sigma}_a)\left\{1 - \left[\frac{kT\ln(\dot{\epsilon}_o/\dot{\epsilon})}{g_o \mu b^3}\right]^{1/q}\right\}^{1/p}, \tag{7}$$

which is a specific form for the more general equation (4). The application of this expression is straightforward; the flow stress is a simple function of the current structure ($\hat{\sigma}$), strain rate and temperature. Evolution of the structure, however, is more difficult to describe; this is the topic of the next Section.

2.2. Structure evolution

Structure evolution is considered as the balance between dislocation accumulation and dynamic recovery and the strain hardening rate $\theta = d\hat{\sigma}/d\epsilon$ is used to characterize the differential variation of the structure parameter with strain. The fundamental relation between the competing processes is written

$$\theta = \theta_o - \theta_r(T, \dot{\epsilon}, \hat{\sigma}), \tag{8}$$

where θ_o is the hardening due to dislocation accumulation and θ_r is the dynamic recovery rate. Applica-

†There is a slight temperature (and pressure) dependence in $\hat{\sigma}$ from $\mu(T, P)$ which, for consistency, will be combined with the s term.

tion of this equation to a variety of f.c.c. pure metals and alloys, using data measured over a wide range of temperatures but a narrow range of strain rates [14], has led to the conclusion that the first term on the right-hand side of equation (8) is roughly constant and equal to $\mu/20$, which is the strain hardening rate during Stage II deformation.

According to the model expressed by equation (8) the important temperature and strain rate dependencies are found in the dynamic recovery term. To proceed with the analysis of this term it is useful to first inspect some characteristics of the strain hardening behavior in f.c.c. metals and alloys. Figure 3 is a schematic representation of the variation of strain-hardening rate with mechanical threshold stress. There are three solid curves shown in this figure, corresponding to three combinations of strain rate and temperature. The strain values for one of the hardening curves, for instance the middle one, given on the top axis indicate that the curve represents the strain hardening behavior to uniaxial strains as high as 2. The θ–σ curves for polycrystalline f.c.c. metals are generally concave up as shown in Fig. 3, but a straight line (dashed line in middle curve) does approximate the behavior over a limited stress or strain range. A linear variation of strain hardening rate with stress indicates Voce behavior,

$$\theta = \theta_o\left[1 - \frac{\hat{\sigma} - \hat{\sigma}_a}{\hat{\sigma}_s(T,\dot{\epsilon}) - \hat{\sigma}_a}\right], \tag{9}$$

where $\hat{\sigma}_s$ is the stress at zero strain hardening rate, sometimes termed the saturation stress. Kocks [13] and Estrin and Mecking [15] have given physical significance to equation (9) by considering the competition between dislocation accumulation and annihilation processes. Estrin and Mecking [15] modified the Voce law to account for dislocation motion in dispersion strengthened or fine-grained materials.

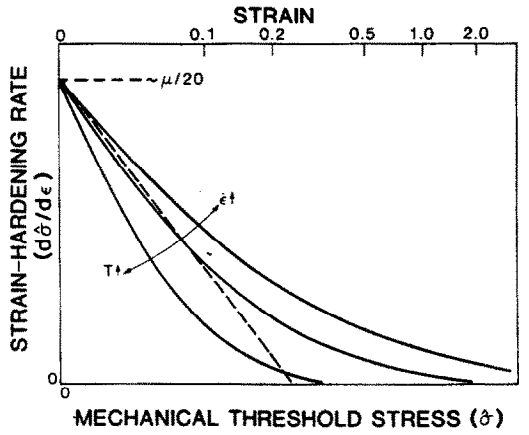

Fig. 3. Schematic illustration of the variation of the strain hardening rate, $\theta = d\hat{\sigma}/d\epsilon$ vs $\hat{\sigma}$ as a function of strain rate and temperature. The dashed line shows Voce law behavior [equation (9)] and the strain scale on the top axis shows that significant deviations from simple Voce behavior occur at large strains.

Most metals do not show Voce behavior over a wide range of stresses, but saturation-like behavior is common. That is, the strain hardening rate continues to decrease toward zero with increasing stress or strain, but true saturation behavior is rarely observed. For this study, we will concentrate on strains <1, assume that the strain hardening curves do saturate, and model the strain hardening behavior using an equation of the form

$$\theta = \theta_o\left[1 - F\left(\frac{\hat{\sigma} - \hat{\sigma}_a}{\hat{\sigma}_s - \hat{\sigma}_a}\right)\right], \tag{10}$$

where the function F is chosen to fit the measured data. In equation (10) as in equation (9) the temperature and strain rate dependencies lie in the saturation threshold stress $\hat{\sigma}_s$.

The strain hardening rate decreases with strain and approaches saturation due to dynamic recovery. At low temperatures in f.c.c. metals, dynamic recovery occurs by cross slip [15], which is both thermally activated and stress assisted. Kocks [13] has proposed a description for $\hat{\sigma}_s(T,\dot{\epsilon})$ that has the same form as that proposed by Haasen [18] for the beginning of dynamic recovery which in turn was based on the calculations by Schoeck and Seeger [19] of the stress dependence of the activation energy for cross slip in f.c.c. metals. The relations is written

$$\ln\left(\frac{\dot{\epsilon}}{\dot{\epsilon}_{so}}\right) = \frac{\mu b^3 A}{kT}\ln\left(\frac{\hat{\sigma}_s}{\hat{\sigma}_{so}}\right), \tag{11}$$

where $\dot{\epsilon}_{so}$, A, and $\hat{\sigma}_{so}$ are constants. The reference stress $\hat{\sigma}_{so}$ is the saturation threshold stress for deformation at 0 K. This expression has been applied by Kocks [13] to the low strain rate, low and elevated temperature deformation of aluminum, copper, and 304L stainless steel and by Haasen [18] to the low strain rate, low temperature deformation of nickel. Equation (11) completes the development of the theoretical model to be used to fit the experimental results described in the following Section.

3. EXPERIMENTAL

Oxygen-free-electronic (OFE) copper (0.9999 Cu) was chosen for this study. Compression specimens were machined from the half-hard stock material and then given a recrystallization anneal at 600°C in vacuum for 1 h to yield the desired well-annealed equiaxed grain structure with an average grain diameter of 40 μm. All of the experiments reported here have been performed in uniaxial compression. Experimental techniques used to measure the flow stress and the mechanical threshold stress have been described previously [1, 2].

In the earlier work, mechanical threshold stress measurements were reported for strain rates from 10^{-4} to $10^4\,s^{-1}$ and for true strains to 25%. Select additional measurements to strains as high as 96% have been added to the test matrix defined above. For

these large strain measurements, the procedure was to incrementally load in steps of ~25% strain followed by relubrication and/or remachining of the solid cylindrical geometry. This minimized the influence of frictional constraint on the specimen as well as the influence of the adiabatic temperature rise for the high strain rate experiments.

3.1. Results at constant structure

The mechanical threshold stress is measured by first deforming several samples identically according to the strain and strain rate history of interest (all histories presented here were produced at ambient temperature) and reloading each sample at various temperatures (<300 K) to measure the yield stress as a function of reload test temperature. The mechanical threshold stress is the flow stress at 0 K, but tests at temperatures <76 K are not performed because contribution from real drag forces can complicate the measured yield stress; thus, an extrapolation to 0 K is required. Equation (7) provides the format needed to perform this extrapolation, which has been described in detail previously [1, 2].

The extrapolated value of the mechanical threshold stress at 0 K depends on the form of the thermal activation law [equation (7)], which differs slightly from that used in earlier work [1, 2] by the inclusion of an athermal stress. The estimated mechanical threshold stress values also depend on the values of p and q chosen in equation (7). In our previous work, these values were chosen as the medians of the ranges given earlier, i.e. $p = \frac{1}{2}$ and $q = \frac{3}{2}$. These values, however, yielded g_o values which we consider to be unrealistic ($g_o \simeq 7$) for dislocation/dislocation interactions. Choosing $p = \frac{2}{3}$ and $q = 1$ led to more plausible values of g_o (to be discussed below). This pair of values corresponds to a random distribution of box-like obstacles [17].

To fit the reload yield stress data to equation (7), the athermal stress was estimated as the yield stress on undeformed material,

$$\hat{\sigma}_a = 40 \text{ MPa}, \tag{12}$$

and was assumed to remain constant with strain. The results of all 41 strain and strain rate histories are listed in Table 1. Included in this table are the measured flow stress and extrapolated mechanical threshold stress and normalized activation energy values. Although as discussed above, the g_o value depends sensitively on the p and q values, the estimated mechanical threshold stress is only weakly dependent on these exponents. In fact, the mechanical threshold stress estimates reported previously for $p = \frac{1}{2}$, $q = \frac{3}{2}$, and $\hat{\sigma}_a = 0$ differ only slightly (<8 MPa) from those reported here ($p = \frac{2}{3}$, $q = 1$, $\hat{\sigma}_a = 40$ MPa).

Most of the reload operations were performed at a strain rate of $1.4 \times 10^{-3}\,\text{s}^{-1}$. In order to evaluate the $\dot{\epsilon}_o$ term in equation (7), additional tests were performed at higher strain rates. The measured flow stress values listed in Table 1 offer another "constant structure" measurement (at the prestrain strain rate). Examples of plots of yield stress (or flow stress for the prestrains) vs test temperature and strain rate are shown in Fig. 4. In these plots the value of $\dot{\epsilon}_o$ has been set at

$$\dot{\epsilon}_o = 10^7\,\text{s}^{-1} \tag{13}$$

which gave the best general agreement for all of the histories. No systematic variation in $\dot{\epsilon}_o$ with history was detected, although it should be emphasized that the low constant-structure strain rate sensitivity in copper makes it difficult to experimentally determine this quantity with precision.

The normalized activation energy is determined from the slope of the line through the data plotted in Fig. 4. Inspection of the results tabulated in Table 1 suggests that there is a slight increase in g_o with increasing $\hat{\sigma}$, which is illustrated in Fig. 5. At low stress there is considerably more variation in the estimate of g_o, due to the almost zero slope at these stresses. However, at higher stresses the confidence in the estimate of g_o is good. To a first approximation we will estimate the normalized activation energy as the average of all the data points (the dashed line in Fig. 5), which gives

$$g_o = 1.6. \tag{14}$$

The significance of the slight increase in g_o with increasing $\hat{\sigma}$ will be discussed in Section 5.

3.2. Application of the results to the description of structure evolution

The key to the successful application of equation (10) to the description of structure evolution is the choice of the function F. Several functions were investigated, including the simple Voce law [equation (10)], the modified Voce law proposed by Estrin and Mecking [15] and a Voce law coupled with a linear strain hardening expression at large strains [20]. To fit the evolutionary equations to the mechanical threshold stress data the factors θ_o and $\hat{\sigma}_s$ were varied iteratively until the lowest error between the experimental data points and the predicted $\hat{\sigma}$–ϵ curve was achieved. The form of the function F finally chosen uses the hyperbolic tangent function and is written as

$$F = \frac{\tanh(2X)}{\tanh(2)} \tag{15}$$

$$\text{where } X = \frac{\hat{\sigma} - \hat{\sigma}_a}{\hat{\sigma}_s - \hat{\sigma}_a}. \tag{16}$$

Combining this expression with equation (10) gives

$$\theta = \theta_o \left[1 - \frac{\tanh(2X)}{\tanh(2)} \right]. \tag{17}$$

A comparison of the best fits of the Voce law [equation (10)], the modified Voce law [15], and equation (17) for the mechanical threshold stress data at $\dot{\epsilon} = 0.015\,\text{s}^{-1}$ is shown in Fig. 6. The agreement between equation (17) and the experimental results is

Table 1. Summary of mechanical threshold stress measurements

$\dot{\epsilon}$ (s^{-1})	ϵ	σ (MPa)	$\hat{\sigma}$ (MPa)		g_o	
			Mean	SE†	Mean	SE†
0.00014	0.05	114	123.1	1.9	2.3	1.4
0.00014	0.10	168	181.1	2.7	2.7	1.4
0.00014	0.15	206	223.2	2.7	2.2	0.7
0.00014	0.20	234	256.9	1.8	2.1	0.4
0.00014	0.25	252	277.6	1.6	2.0	0.2
0.00014	0.468	309	340.2	1.8	1.8	0.2
0.015	0.05	118	127.1	2.5	1.8	1.1
0.015	0.10	175	188.5	2.7	2.2	0.8
0.015	0.15	218	234.3	1.6	2.0	0.3
0.015	0.20	247	268.0	2.4	1.9	0.3
0.015	0.25	269	291.8	2.4	2.0	0.3
0.015	0.491	336	367.3	2.2	1.7	0.2
0.015	0.96	402	435.8	2.1	1.3	0.1
0.82	0.05	127	135.9	4.2	1.6	1.7
0.82	0.10	180	192.5	1.6	2.3	0.5
0.82	0.15	224	244.2	2.2	2.0	0.4
0.82	0.20	268	281.7	1.9	1.6	0.2
0.82	0.25	295	305.7	2.2	1.6	0.2
0.82	0.521	354	396.8	2.5	1.2	0.1
0.82	0.727	381	432.2	1.7	1.1	0.1
81	0.05	130	134.7	3.0	1.1	0.4
81	0.10	194	203.1	1.6	1.3	0.2
81	0.15	241	250.3	1.9	1.8	0.3
81	0.20	281	295.0	1.4	1.5	0.1
81	0.25	307	324.2	1.6	1.5	0.1
1800	0.064	144	173.8	3.3	2.3	1.6
1800	0.107	203	219.1	1.0	2.7	0.3
1800	0.152	252	275.6	1.8	1.3	0.1
1800	0.209	299	305.0	1.7	1.6	0.1
1800	0.253	319	340.0	1.0	1.2	0.1
1800	0.52	415	441.9	2.8	1.0	0.1
5000	0.065	157	180.6	1.5	2.9	0.9
5000	0.10	206	227.9	2.2	1.8	0.4
5000	0.168	277	281.7	1.4	1.4	0.1
5000	0.211	309	319.0	1.0	1.3	0.1
5000	0.257	332	350.1	1.9	1.1	0.1
9500	0.087	205	211.6	1.6	2.4	0.4
9500	0.134	259	269.5	1.5	1.5	0.1
9500	0.156	280	294.7	2.0	1.3	0.1
9500	0.189	308	320.8	1.6	1.1	0.1
9500	0.226	330	337.0	0.8	1.3	0.1

†Standard error of estimate.

far better than that obtained with the Voce and modified Voce laws, which is why equation (17) was chosen over the more physically based laws.

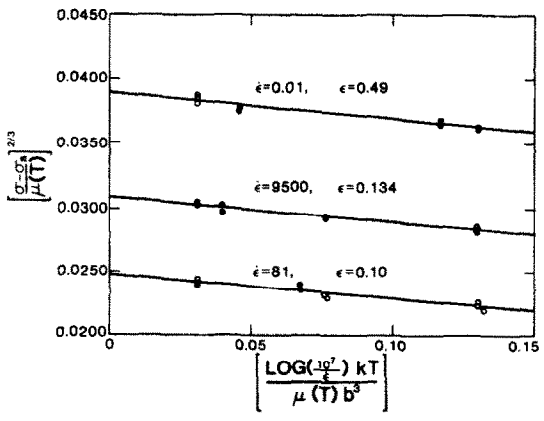

Fig. 4. Reload yield stress (open circles) vs test temperature on samples predeformed as indicated. The results are plotted according to equation (7) with $\hat{\sigma}_a = 40$ MPa, $p = \frac{2}{3}$, $q = 1$ and $\dot{\epsilon}_o = 10^7\,s^{-1}$. The solid circles give yield stress or flow stress measured at strain rates other than that used for the open circles ($\dot{\epsilon} = 0.0015\,s^{-1}$).

We emphasize that the particular evolution law chosen to fit the results presented here [equation (17)] is merely a convenient mathematical form which happens to describe the data. Although it is satisfying that equation (17) approximates the Voce law at low strains, we imply *no* physical significance to the

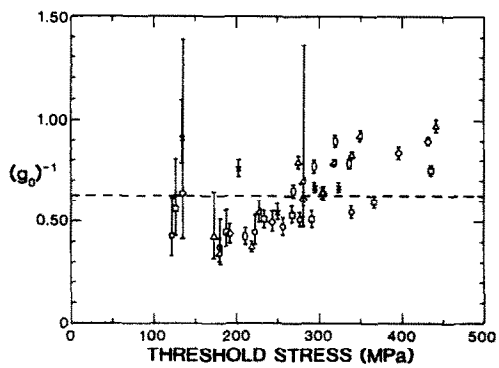

Fig. 5. Inverse of the normalized activation energy [equation (6)] vs mechanical threshold stress. The dashed line shows the mean value, $g_o = 1.6$. The symbols show data at the strain rates identified in the key of Fig. 7.

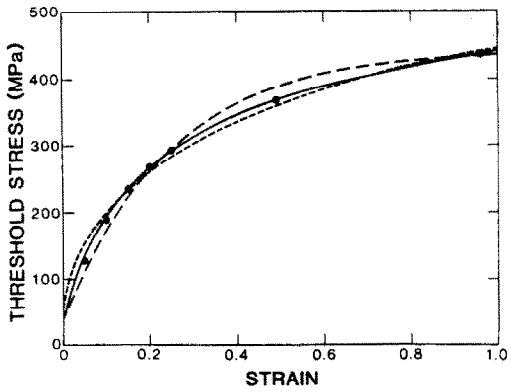

Fig. 6. Fit of equation (17) (solid line), the Voce law [equation (9)] (long dashed line) and the modified Voce law of Estrin and Mecking [15] (short dashed line) to the mechanical threshold data for deformation at $\dot{\epsilon} = 0.015\,s^{-1}$.

particular form of the fit expressed by equation (17), and in fact doubt that the same evolution law would fit data in other f.c.c. metals and alloys as well as it is found to fit data in copper. Hopefully, more universal, physically based evolution laws will arise as the fundamental understanding of texture evolution and Stage IV deformation are advanced.

The fit of equation (17) to the mechanical threshold stress data at all the strain rates is shown in Fig. 7, and the values of $\hat{\sigma}_s$ and θ_o for the seven curves shown in Fig. 7 are listed in Table 2. The fitted curves at strain rates of 1.4×10^{-4}, 1.5×10^{-2}, 0.82 and $2 \times 10^{3}\,s^{-1}$ represent actual best fits to equation (17). Data at the three other strain rates ($81\,s^{-1}$, 5×10^{3} and $9.5 \times 10^{3}\,s^{-1}$) were limited to strains of 25% and less, which is not a sufficiently wide strain range to give a meaningful "best fit" to equation (17). For these data, the saturation threshold stress results for the first four strain rates were first plotted according to equation (11) as shown in Fig. 8. The data points are well described by a line, which gives confidence in the specific form of the model chosen to represent dynamic recovery [equation (11)]. The line in Fig. 8

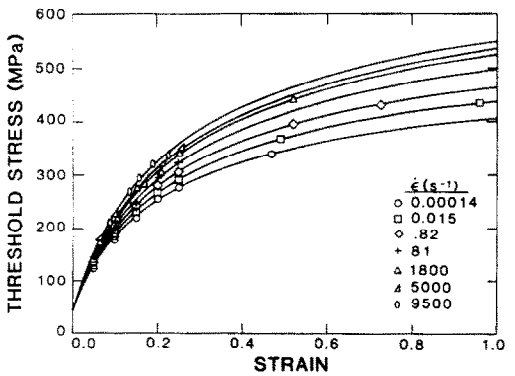

Fig. 7. Fit of equation (17) to mechanical threshold stress data at all of the strain rates.

Table 2. Evolution law parameters

$\dot{\epsilon}$ (s^{-1})	$\hat{\sigma}_s$ (MPa)	θ_o (MPa)
0.00014	482	2293
0.015	530	2305
0.82	564	2425
81	617	2456
1800	655	2550
5000	666	2634
9500	674	2840

defines the saturation threshold stress values for the three remaining strain rates. The θ_o values listed in Table 2 for these strain rates represent the best fits of equation (17) to the threshold stress data with the specified saturation threshold stresses.

As described previously, the mechanical threshold stress measurements were performed only on samples given stress and strain rate histories at ambient temperature. Thus, the data required to best evaluate the constant $\hat{\sigma}_{so}$ in equation (11) is unavailable. However, stress–strain curves to strains as large as 1 were performed at 76 K and from these data the value of $\hat{\sigma}_{so}$ was estimated as

$$\hat{\sigma}_{so} = 900\ \text{MPa}. \tag{18}$$

The two remaining constants in equation (11) assume values of

$$A = 0.31 \tag{19}$$

and

$$\dot{\epsilon}_{so} = 6.2 \times 10^{10}\,s^{-1}. \tag{20}$$

The results listed in Table 2 show a definite strain rate dependence of the Stage II hardening rate θ_o, which is in contrast to the expected behavior. [Note that there was no strain rate dependency of θ_o suggested in equations (8), (9), and (10)]. Figure 9 shows the variation of θ_o with strain rate. The curve fit to these data points has the form

$$\theta_o(\text{MPa}) = 2390 + 12.0 \ln(\dot{\epsilon}) + 0.034\,\dot{\epsilon}. \tag{21}$$

where $\dot{\epsilon}$ is in units of s^{-1}. The term which is linear in strain rate is significant because it has a strong

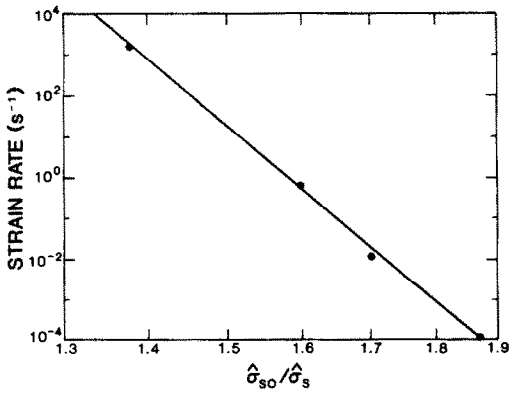

Fig. 8. Variation of the saturation mechanical threshold stress (on logarithmic axis) with strain rate for data at $\dot{\epsilon} = 0.00014$, 0.015, 0.82 and $1800\,s^{-1}$ and fit to equation (11).

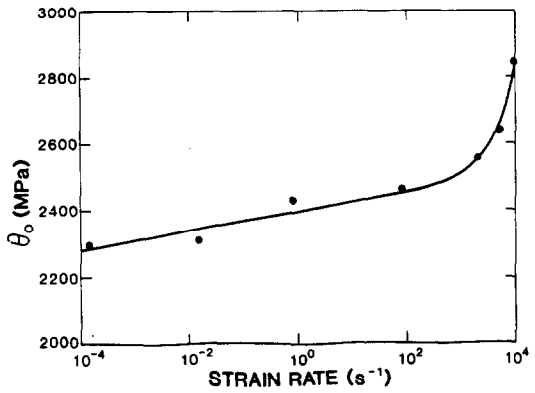

Fig. 9. Variation of $\hat{\sigma}_o$ [equation (17)] with strain rate and fit to equation (21).

influence at high strain rates. This observed behavior will be discussed further in Section 5.

4. PREDICTIONS OF THE MODEL

Equation (17) together with equation (11) [with constants given in equations (18), (19), and (20) and summarized in Table 3] and equation (21) constitute the evolutionary description for copper. The variation of $\hat{\sigma}$ with ϵ is found by integrating equation (17) along the prescribed temperature and strain rate path. For monotonic (and isothermal) loading, a direct integration of equation (17) gives

$$\epsilon = \frac{-13.2(\hat{\sigma}_s - \hat{\sigma}_a)}{\theta_o} \times \{X + 0.52\ln[-1.04\sinh(2X) + \cosh(2X)]\}. \quad (22)$$

However, the differential form [equation (17)] is more useful for arbitrary strain rate and temperature paths. At any instant the value of the flow stress is computed using equation (7) with the constants $\hat{\sigma}_a$, $\dot{\epsilon}_o$, and g_o given by equations (12), (13), and (14) and summarized in Table 3.

Predictions of the model and comparisons with experimental results for room temperature deformation at strain rates of 0.015 and $8500\,s^{-1}$ are shown in Fig. 10. The prediction at the higher strain rate is made for both isothermal (295 K) and adiabatic conditions. For the latter condition the temperature is calculated assuming 95% of the work of plastic deformation is converted into heat which results in a temperature rise according to

$$T = T_0 + \frac{0.95}{\rho c_p}\int_0^e s(e)\,de, \quad (23)$$

†The pressure-shear experimental curves shown in Fig. 11 are recent results which do not appear in [22] but have been supplied by R. J. Clifton, Division of Engineering, Brown University, Providence, R.I. A conversion factor of $\sqrt{3}$ has been used to convert shear stress–shear strain to axial stress–axial strain.

Table 3. Constants in thermal activation and structure evolution laws

Constant	Relevant equation(s)	Value
$\hat{\sigma}_a$	(7), (16)	40 MPa
p	(7)	2/3
q	(7)	1
$\dot{\epsilon}_o$	(7)	$10^7\,s^{-1}$
g_o	(7)	1.6
$\dot{\epsilon}_\infty$	(11)	$6.2 \times 10^{10}\,s^{-1}$
A	(11)	0.312
$\hat{\sigma}_\infty$	(11)	900 MPa
k/b^3	(7), (11), (31)	0.823 MPa K^{-1}

where s and e are the engineering stress and strain, ρ is the density, and c_p is the heat capacity. The low strength and high value of ρc_p for copper make the correction for adiabatic deformation small, but as shown in Fig. 10, the correction does bring the prediction into closer agreement with the experimental data. Flow stress data at strains $\lesssim 5\%$ for the dynamic curve are not shown in this plot (or in subsequent plots) because the split Hopkinson pressure bar experimental technique is inherently inaccurate at low plastic strains [21].

The comparisons in Fig. 10 show good agreement between predictions of the model and the experimental results. However, the model was fit to data obtained for room temperature deformation between strain rates of 10^{-4} and $10^4\,s^{-1}$, and comparisons made within this fitted regime are not a stringent test of the modeling procedure. A more critical test of the general validity of the model is to test it at conditions outside this regime. Two such comparisons are given in Fig. 11, which shows predictions of the model and experimental results for a test at 473 K and a strain rate of $5000\,s^{-1}$ and for two tests at room temperature and a strain rate of $\sim 6.4 \times 10^5\,s^{-1}$ from measurements of Huang and Clifton using the pressure-shear experiment [22]†. The fit in Fig. 11(a) is quite satisfactory. In Fig. 11(b) the model prediction for the latter condition exceeds the measurements; however, the difference between the predicted and measured flow stress levels could easily be due to the difference in stress state between the two experiments. Experience at low strain rates shows that the flow stress is uniaxial deformation at a von Mises equivalent strain of 0.8 typically exceeds that in shear by ~15–20% [23]. Thus, the comparisons between the predictions of the model and the experimental results in Fig. 11 are close, especially when it is emphasized that the conditions are extrapolations outside the conditions over which the model has been fit.

4.1. Strain-rate change tests

The modeling procedure described in Section 2 is easily applied to the case of a strain rate change test. Strain rate influences the saturation flow stress through equation (11), the initial strain hardening rate through equation (21), and the instantaneous ratio of the flow stress to the mechanical threshold

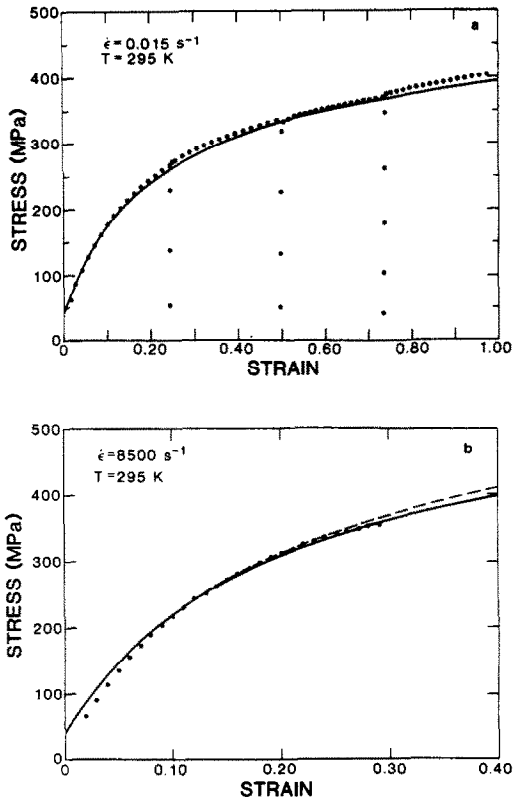

Fig. 10. Predictions of the model expressed by equations (17), (11) and (7) and comparisons with experimental results for (a) $\dot{\epsilon} = 0.015\,s^{-1}$ and (b) $\dot{\epsilon} = 8500\,s^{-1}$. The calculations for the latter strain rate are for both isothermal ($T = 295$ K, dashed line) and adiabatic deformation (solid line).

stress through equation (7). For the application of the model to monotonic loading at constant strain rate and temperature, the values of θ_o and $\hat{\sigma}_s$ do not vary. In a strain rate or temperature change test, however, these values must be updated whenever a change in $\dot{\epsilon}$ or T is specified. The adiabatic calculations shown in Figs 10 and 11, for instance, require small changes to $\hat{\sigma}_s$ after each strain increment.

Comparisons of predictions of the model with results from strain rate-jump tests are shown in Fig. 12. These measurements show the measured stress–strain curves for deformation at $\dot{\epsilon} = 2500\,s^{-1}$ following deformation at $\dot{\epsilon} = 1.4 \times 10^{-1}\,s^{-1}$ to a strain ϵ_c and unloading. Close agreement between predictions of the model and the measured behavior is found for a strain rate change at low values of ϵ_c, but as ϵ_c increases, the measured curves approach the higher strain rate flow stress level more rapidly than is predicted. The failure of a single-parameter model, such as the one studied in this investigation, to fully account for transient behavior following an abrupt change in strain rate has been noted previously [14].

The model prediction and experimental result for a strain rate reduction from $\dot{\epsilon} = 2500$ to $0.0015\,s^{-1}$ at $\epsilon_c = 0.52$ are shown in Fig. 13. All calculations for the high strain rate are performed assuming adiabatic deformation, whereas the deformation is assumed to be isothermal for the low strain rate. The deformation at the dynamic strain rate was performed in two increments. Thus, there is a very slight kink in the predicted curve at $\epsilon = 0.25$ which corresponds to the return of the temperature from 311 to 295 K between loading increments. The solid curve following the strain rate reduction overestimates the measured data considerably. We believe that this is due to the variation of g_o with strain rate noted in Fig. 5. When the experimentally measured value (from Table 1, $g_o = 1.0$ at $\dot{\epsilon} = 1800\,s^{-1}$ and $\epsilon = 0.52$) is used following the strain rate change, the agreement (dashed curve in Fig. 13) between the predicted and measured behavior is improved. Note, however, that accounting for the slight variation of g_o with strain would not improve the agreement between the predicted and measured behavior in Fig. 12. Implications of the variation of g_o with strain rate are discussed in the following Section.

5. DISCUSSION

There are two results of these experiments and of the associated theoretical modeling that require discussion. The first result is the dramatically increased initial strain hardening rate that is observed at high

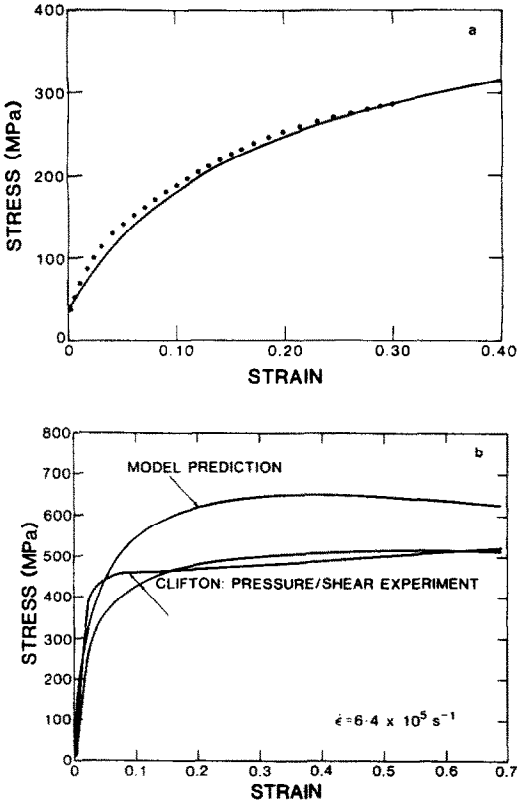

Fig. 11. Predictions of the model and comparisons with experimental results for (a) $\dot{\epsilon} = 5000\,s^{-1}$ and $T = 473$ K and (b) $\dot{\epsilon} = 6.4 \times 10^5\,s^{-1}$ and $T = 295$ K [22].

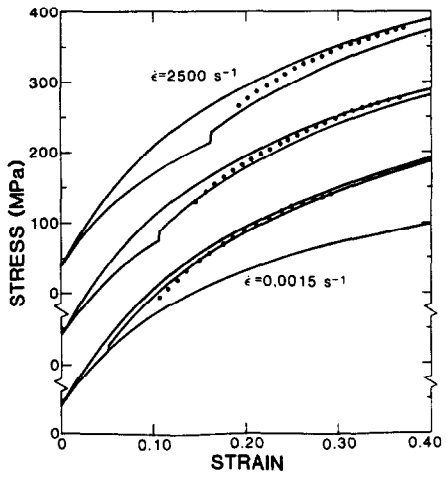

Fig. 12. Predictions of the model and comparisons with experimental results for a strain rate change from $\dot{\epsilon} = 0.0015\,s^{-1}$ to $\dot{\epsilon} = 2500\,s^{-1}$ at strains of $\epsilon = 0.0513$, 0.1054 and 0.1625.

strain rates. The second result is the noted variation of the normalized activation energy.

5.1. *Initial strain hardening rate*

A fundamental supposition of Mecking and Kocks is that the initial portion of the stress–strain curve is affected strongly (almost solely) by the athermal dislocation accumulation rate whereas the large strain regime of the stress–strain curve is affected strongly (almost solely) by the dislocation rearrangement and therefore the saturation flow stress behavior. These features are unaltered by the details of the evolutionary law, i.e. whether this is assumed to be the Voce, modified Voce [14], or the particular law chosen for this study. The mechanical threshold stress data listed in Table 1 and shown in Fig. 7 show an unusually large strain rate dependence at low strains. This behavior cannot be described by equation (10) unless the initial strain hardening rate is allowed to vary with strain rate. Thus, the observed variation of θ_o with $\dot{\epsilon}$ is not a function of the particular evolutionary law chosen; it instead indicates a general and unique finding which has not been noted previously, at least in the context of the basic model represented by equation (10).

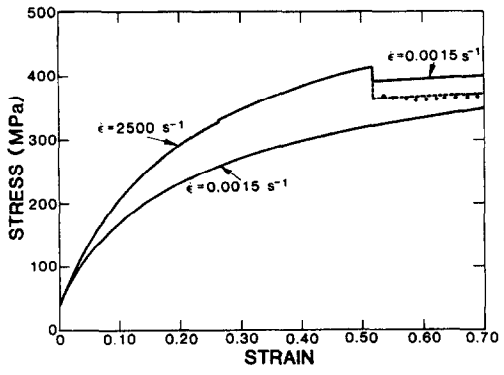

Fig. 13. Prediction of the model and comparison with experimental result for a strain rate change from $\dot{\epsilon} = 2500$ to $0.0015\,s^{-1}$ at $\epsilon = 0.52$. Solid line shows model predictions for $g_o = 1.6$ whereas dashed line shows model prediction for $g_o = 1$, which is the actual value measured at $\dot{\epsilon} = 1800\,s^{-1}$ and $\epsilon = 0.52$ and listed in Table 1.

The variation of the initial strain hardening rate with strain rate was illustrated in Fig. 9. Although the magnitude of the variation in θ_o over the strain-rate range of these experiments is only 24%, the linear dependence on $\dot{\epsilon}$ at high strain rates has a dramatic effect as the strain rate is raised above $10^4\,s^{-1}$. This was demonstrated in the prediction at a strain of $6.4 \times 10^5\,s^{-1}$ shown in Fig. 11. The rapid strain hardening and approach to saturation behavior computed at this strain rate seem unusual, but the predictions are supported by the experimental data at this strain rate.

The recent modification to the Voce law proposed by Estrin and Mecking [15] provides a hint of how the strain rate could influence the initial strain hardening rate. Physical significance has been given to the Voce law by modeling the competition between dislocation accumulation and dynamic recovery and assuming for the former that dislocations become immobilized and thus are stored after traveling a distance proportional to the average distance between dislocations [13]. This leads to the constant initial strain hardening rate, $\theta_o \simeq \mu/20$. To account for dislocation storage in very fine grained materials or dispersion strengthened materials, Estrin and Mecking reasoned that the dislocation immobilization distance d should remain constant, which leads to an initial strain hardening rate $\theta_o \propto \mu^2/d\sigma$. For the cases considered by Estrin and Mecking, the constant d would not be expected to vary. At very high strain rates, however, it might be speculated that the dislocation immobilization distance is simply the distance that a dislocation can move during the imposed time duration of the deformation. This distance would be inversely proportional to the imposed strain rate, which would give the linear strain rate dependence of θ_o suggested by the measurements reported here.

The coefficient on the term linear in strain rate in equation (21) was estimated as 0.034. This suggests that the linear term begins to dominate the θ_o value at strain rates as low as $10^5\,s^{-1}$. An estimate of the strain rate at which the dislocation storage distance falls below the average spacing between dislocations follows from setting the dislocations multiplication rates for the two processes equal.

$$K(\rho)^{1/2} = \frac{1}{bd}, \tag{24}$$

where the left-hand term is $d\rho/d\epsilon$ when dislocations become stored upon traveling the average distance between dislocations ($K \simeq 2\theta_o/\mu b$) and the right-hand term is $d\rho/d\epsilon$ when the storage distance is constant and equal to d (which we will allow to vary

with strain rate). Substituting for $\rho^{1/2}$ the well-known relationship between flow stress and forest dislocation density,

$$\sigma \simeq \mu b \rho^{1/2} \tag{25}$$

and for d the product of the average dislocation velocity in free glide,

$$v = \frac{\sigma b}{MB}, \tag{26}$$

where M is a Taylor factor and B is the drag coefficient, and an appropriate time, which is the strain divided by the strain rate, gives

$$\frac{2\theta_o \sigma}{\mu^2} = \frac{MB\dot{\epsilon}}{\sigma\epsilon}. \tag{27}$$

When typical values for all the constants ($\theta_o = 2000$ MPa, $B = 4 \times 10^{-5}$ Pa s^{-1} [2], $M = 3$, and $\mu = 42$ GPa) are inserted, the estimated strain rate above which the storage distance falls below the average spacing between dislocations at yield is $\dot{\epsilon} = 3 \times 10^4$ s^{-1}. That this estimate agrees with the measured result supports the speculation that at high strain rates the distance a dislocation can travel begins to define the average storage distance, which determines the dislocation generation rate.

The limiting travel distance described above has a strong strain rate dependence, but this is not coupled to temperature dependence by way of an Arrhenius law as is normally found in metallurgical processes. The temperature dependence arises only through $B(T)$ and $\mu(T)$; the latter dependence is typical of athermal hardening in general. This is consistent with the fact that investigations at low strain rates but very low temperatures [24] have not led to the suggestion of the dramatically increased athermal hardening rate found at high strain rates and ambient temperature.

Our observation of the strain rate dependent initial strain hardening rate, and the accompanying strain rate dependent dislocation accumulation rate, is made indirectly from measurements of the mechanical threshold stress, rather than directly from, for instance, dislocation density measurements in the transmission electron microscope. As noted above, however, the actual magnitude of change in mechanical threshold stress is small over the strain rate range of our experiments. For example, at 5% strain, where the change in $\hat{\sigma}$ should be primarily due to the change in θ_o, the ratio of the highest to the lowest mechanical threshold stress [from Fig. 7 or equation (22)] is only 1.19. This implies from equation (25) that the total dislocation densities should differ by only 1.42. The microstructures at even this low a strain level are heavily dislocated ($\rho \simeq 5 \times 10^{13}$ m^{-2}) and the precision of microscopic techniques is insufficient to measure with confidence such a small difference in dislocation density. However, Edington [25] reported slightly increased dislocation densities in single crystals of copper deformed at strain rates up to $\sim 4 \times 10^3$ s^{-1} than found in samples deformed at quasi-static strain rates to the same plastic strains.

There is additional evidence at even higher strain rates that the dislocation accumulation rate in copper becomes rapid. This evidence comes from experiments in the shock-wave regime, which typically yield strain rates of 10^6–10^8 s^{-1}. Dislocation density measurements reported by Murr [26] in shock-deformed copper showed significantly increased dislocation generation at these very high strain rates. Brillhart *et al.* [27] measured increased dislocation generation and stored energy in shock-loaded copper†. These measurements are consistent with the mechanical threshold measurements and microstructural observations by Follansbee and Gray on shock-deformed copper [28]. Clearly, a picture of enhanced dislocation accumulation and structure evolution at high strain rates is emerging, even though the mechanisms leading to these events are still speculative.

5.2. *Variation of the normalized activation energy*

The estimates of g_o noted in Fig. 5 are made from the slope of the fits through the reload yield stress data, as illustrated in Fig. 4. In Fig. 4 the value of $\dot{\epsilon}_o$ has been set at 10^7 s^{-1}. For reload experiments at constant strain rate but variable temperature, the $\dot{\epsilon}_o$ value does not have to be prescribed; the convenient combination of parameters for the abscissa then becomes $(kT/\mu b^3)^{1/q}$ and the measured slope S on these coordinates is proportional to both g_o and $\log(\dot{\epsilon}_o/\dot{\epsilon})$,

$$S = \left(\frac{\hat{\sigma} - \hat{\sigma}_o}{\mu(T)}\right)^p \frac{\log(\dot{\epsilon}_o/\dot{\epsilon})}{g_o}. \tag{28}$$

That is, changes in both $\dot{\epsilon}_o$ and g_o contribute to departures from assumed (i.e. g_o and $\dot{\epsilon}_o$ constant) behavior. It is evident in equation (28), however, that because $\dot{\epsilon}_o$ is within a logarithmic term, very much larger changes in $\dot{\epsilon}_o$ are required to achieve the same effects as from small changes in g_o. Roughly a factor of 2 variation in g_o is found when $\dot{\epsilon}_o$ is assumed constant (see Fig. 5). For the same change in S the $\dot{\epsilon}_o$ term would have to vary by a factor of 10^5. It is possible to explain small changes (of the order 10) in $\dot{\epsilon}_o$ due to variations in the mobile dislocation density ρ_m and average spacing between obstacles d according to

$$\dot{\epsilon}_o \propto \rho_m d. \tag{29}$$

However, a variation of the order 10^5 seems unlikely. In addition, because reload yield stress (and flow stress) data are available as a function of strain rate as well as temperature, the $\dot{\epsilon}_o$ value can be estimated, and, as noted earlier, examination of the data led to no suggestion of such a large variation in $\dot{\epsilon}_o$. It is likely that both changes in $\dot{\epsilon}_o$ and in g_o contribute to

†A correction for deformation twinning led these investigators to conclude that stored energy, but not dislocation density, is higher in shock-deformed material than in quasi-statically deformed material.

the observed behavior, but the former probably can be neglected in comparison with the latter.

The increase in g_o with stress noted in Fig. 5 is consistent with previous observations; this behavior has been described as indicating departure from Cottrell–Stokes (C–S) behavior [29], which, in the context of equation (7), requires that g_o remain constant. Violation of C–S behavior in single crystal and polycrystalline copper has been well documented [30–32]. The C–S law is generally obeyed at low strains, particularly in Stage II deformation of single crystals [33]. Deviations occur as the strain is increased, and as the temperature is raised the strain at the onset of deviations decreases. This might suggest that at high strain rates deviations from C–S behavior would occur at larger strains, but the inverse is suggested by the results in Fig. 5.

Mecking and Kocks [14] have suggested that the quantity which correlates with deviations from the C–S law is the dynamic recovery rate [equation (8)]

$$\theta_r(\hat{\sigma}, \dot{\epsilon}, T) = \theta_o(\dot{\epsilon}) - \theta(\hat{\sigma}, \dot{\epsilon}, T). \tag{30}$$

This correlation is claimed to be due to a "recovery strain (rate)" that is associated with the rearrangement of dislocations within cell walls, which is the primary mechanism for dynamic recovery. At high strain rates the strain rate dependence of the athermal hardening rate θ_o rises, which leads to accelerated structure evolution and higher dynamic recovery rates than found at quasi-static strain rates. This trend is consistent with the stronger departures from C–S behavior observed when the strain rate is raised above $\sim 10^3\,s^{-1}$.

Another possibility for the observed departure from C–S behavior is that a different type of obstacle begins to contribute to the controlling deformation mechanism. We assume in copper that the predominant obstacles are forest dislocations and that the rate sensitivity is defined by the kinetics of the interaction between mobile dislocations and these obstacles. Indeed the average g_o measured is consistent with such a mechanism; this is seen by evaluating the strain rate sensitivity parameter m,

$$m = \frac{\partial \ln \dot{\epsilon}}{\partial \ln \sigma} = \frac{g_o \mu(T) b^3}{kT} pq\, X^p [1 - X^p]^{q-1}, \tag{31}$$

where

$$X = \frac{\sigma - \hat{\sigma}_a}{\hat{\sigma} - \hat{\sigma}_a}.$$

For typical values ($X = 0.91$) the m-value calculated from equation (31) gives $m = 173$, which is close to the value reported previously for dislocation–dislocation interactions [14]. At large strains this m value is observed to decrease; this would occur if another, more rate-sensitive obstacle were introduced. It can be speculated, for instance, that the interaction of dislocations with deformation produced vacancies would yield an increased strain rate sensitivity. However, a dramatically increased vacancy or loop density has not been reported by those performing microstructural evaluations of copper deformed to large strains or at high strain rates [25, 34, 35].

The detailed analysis of deviations from C–S behavior is beyond the scope of the present work. Fortunately, the deviations are slight. As shown in Figs 10–12 the assumption that g_o remains constant is sufficient for many of the predictions, particularly at low strains. For calculations at large strains and high strain rates, however, it may be necessary to incorporate the actual variation of g_o with mechanical threshold stress and strain rate.

6. CONCLUSIONS

The uniaxial deformation behavior of copper over a wide range of strain rates has been described using a single parameter internal state variable model. The foundation of the model is the separation of the constant-structure part of the strain rate sensitivity from the structure evolution part. These are fundamentally different processes which require different theoretical models. A combination of physically based [i.e. equations (7) and (11)] and phenomonologically based [equation (17)] expressions to describe these processes has been applied and fitted to mechanical threshold stress measurements from strain rates of 10^{-4}–$10^4\,s^{-1}$ and for strains to ~ 1.

The major conclusion of this work is that there is strong evidence that the dislocation accumulation rate, or Stage II hardening rate, begins to increase dramatically with strain rate at strain rates exceeding $\sim 10^3\,s^{-1}$. This observation explains the origin of the "increased strain rate sensitivity" of the flow stress at constant strain found in copper and other f.c.c. metals at these high strain rates. A simple mechanism for the increased strain hardening, based on a velocity-limited dislocation storage distance, has been proposed. One interesting implication of this finding is that at strain rates exceeding $\sim 10^5\,s^{-1}$ the strain hardening will quickly saturate and the stress–strain behavior will approach perfect plasticity. The reason for this is that the strain rate sensitivity of the athermal hardening rate exceeds the strain rate sensitivity of the saturation stress at high strain rates. There is limited experimental evidence which supports this prediction. The measurements of Huang and Clifton [22] at a strain rate of $6.4 \times 10^5\,s^{-1}$ shown in Fig. 11 provide one example of the rapid structure evolution and saturation of strain hardening at high strain rates. Another example is found in recent measurements by Sobolenko and Teslenko of the yield stress of repeatedly shock-deformed Al–6%Mg [36]. These investigators measured a 73% increase in yield strength following the first shock loading increment at 6 GPa but only a 5% total further increase for up to four additional shock loading increments.

A second conclusion of the work is that, as noted by previous investigators, the constant-structure strain rate sensitivity is not well described by the Cottrell–Stokes law. Deviations from this law appear to increase at high strain rates (as $\theta \to 0$). Physically based and generally agreed upon analytical descriptions for these deviations are not currently available. We noted that the strain rate dependence of the deviation from the C–S law was consistent with the concept of a "recovery strain" contribution due to dynamic recovery, but that the addition of a second, shorter-range obstacle could also lead to the observed behavior. Fortunately, to a first approximation, these deviations can be ignored; but the detailed $g_o(\dot{\sigma})$ variation should be incorporated into the model, either with tabular or empirical formats, for the best predictions.

Comparison of the predictions of the model with experimental results showed good agreement. Also, extrapolations of the model to conditions outside of the regime where the model was fitted compared well with available experimental results. Predictions for the behavior following strain rate change tests agreed with measurements at low strains but deviated noticeably at large strains. This supports the general modeling procedure and demonstrates that a simple, single-parameter model, which naturally accounts for history effects, can be used to describe the deformation of copper over a wide range of strain rates. The single-parameter model described here is more successful in describing monotonic deformation than transient deformation, and this will be the case until the mechanism leading to the enhanced hardening following a strain rate change is determined. Addition of a new mechanism such as this into the modeling procedure outlined here will likely require the introduction of an additional state parameter.

Acknowledgements—The authors would like to acknowledge the contributions of W. J. Wright to the split Hopkinson pressure bar measurements and M. F. Lopez to the mechanical threshold stress measurements. This research was supported by the U.S. Department of Energy, Office of Basic Energy Sciences, Division of Materials Sciences.

REFERENCES

1. P. S. Follansbee, *Metallurgical Applications of Shock-Wave and High-Strain-Rate Phenomena* (edited by L. E. Murr, K. P. Staudhammer and M. A. Meyers), p. 451. Marcel Dekker, New York (1986).
2. P. S. Follansbee, G. Regazzoni and U. F. Kocks, *Mechanical Properties of Materials at High Rates of Strain*, Inst. Phys. Conf. Ser. 70, The Institute of Physics, 71 (1984).
3. A. Kumar, F. E. Hauser and J. E. Dorn, *Acta metall.* **16**, 1189 (1968).
4. A. V. Granato, *Metallurgical Effects at high Strain Rates* (edited by R. W. Rohde, B. M. Butcher, J. R. Holland and C. H. Karnes), p. 255. Plenum Press, New York (1973).
5. R. A. Frantz and J. Duffy, *J. appl. Mech.* **39**, 939, 1972.
6. T. Glenn and W. Bradley, *Metall. trans.* **4**, 2343 (1973).
7. J. R. Klepaczko, *Mat. Sci. Engng* **18**, 121 (1975).
8. P. E. Senseny, J. Duffy and H. Hawley, *J. appl. Mech.* **45**, 60 (1978).
9. J. Lipkin, J. D. Campbell and J. C. Swearengen, *J. Mech. Phys. Solids* **26**, 251 (1978).
10. J. R. Klepaczko and C. Y. Chiem, *J. Mech. Phys. Solids* **34**, 29 (1986).
11. M. F. Kanninen, A. K. Mukherjee, A. R. Rosenfield and G. T. Hahn, *Mechanical Behavior of Materials under Dynamic Loads* (edited by U. S. Lindholm), p. 96. Springer, New York (1968).
12. J. W. Taylor, F. H. Harlow and A. A. Amsden, *J. appl. Mech.* **45**, 105 (1978).
13. U. F. Kocks, *J. Engng Mater. Technol.* **98**, 76 (1976).
14. H. Mecking and U. F. Kocks, *Acta metall.* **29**, 1865 (1981).
15. Y. Estrin and H. Mecking, *Acta metall.* **32**, 57 (1984).
16. G. Regazzoni, U. F. Kocks and P. S. Follansbee, *Acta metall.* (1987). To be published.
17. U. F. Kocks, A. S. Argon and M. F. Ashby, *Thermodynamics and Kinetics of Slip*, Prog. Mater. Sci. 19, Pergamon Press, New York (1975).
18. P. Haasen, *Phil. Mag.* **3**, 384 (1958).
19. G. Schoeck and A. Seeger, *Defects in Crystalline Solids*, Physical Society, London (1955).
20. C. Tome, G. R. Canova, U. F. Kocks, N. Cristodoulou and J. J. Jonas, *Acta metall.* **10**, 1637 (1984).
21. P. S. Follansbee, *Metals Handbook, 9th edn*, Vol. 8, p. 198. Am. Soc. Metals, Metals Park, Ohio (1985).
22. S. Huang and R. J. Clifton, to appear in *Proc. of the IUTAM Symp. on Macro- and Micro-Mechanics of High Velocity Deformation and Fracture*, Tokyo, Japan (1985).
23. S. S. Hecker and M. G. Stout, *Deformation, Processing, and Structure* (edited by G. Krauss), p. 1. Am. Soc. Metals, Metals Park, Ohio (1984).
24. F. P. Bullen and M. M. Hutchison, *Phil. Mag.* **8**, 461 (1963).
25. J. W. Edington, *Phil. Mag.* **19**, 1189 (1969).
26. L. E. Murr, *Shock-Wave and High-Strain-Rate Phenomena in Metals* (edited by M. A. Meyers and L. E. Murr), p. 607. Plenum Press, New York (1981).
27. D. C. Brillhart, R. J. De Angelis, A. G. Preban, J. B. Cohen and P. Gordon, *Trans. A.I.M.E.* **239**, 836 (1967).
28. P. S. Follansbee and G. T. Gray, *Shock Waves in Condensed Matter* (edited by Y. M. Gupta), p. 371. Plenum Press, New York (1986).
29. A. H. Cottrell and R. J. Stokes, *Proc. R. Soc. A* **233**, 17 (1955).
30. F. P. Bullen and C. B. Rogers, *Phil. Mag.* 9, 401 (1964).
31. F. P. Bullen and S. McK. Cousland, *Phys. Stat. Sol.* **27**, 501 (1968).
32. R. Zeyfang, O. Buck and A. Seeger, *Phys. Stat. Sol.* **61b**, 551 (1974).
33. H. Mecking and K. Lucke, *Mater. Sci. Engng* **1**, 349 (1967).
34. M. F. Stevens and P. S. Follansbee, *Proc. 44th Annual Meeting of the Electron Microscopy Society of America* (edited by G. W. Bailey), p. 420. San Francisco Press, San Francisco, Calif. (1986).
35. J. C. Giannota, G. Regazzoni and F. Montheillet, *Strength of Metals and Alloys, 7th Int. Conf.* (edited by H. J. McQueen, J. P. Bailon, J. I. Dickson, J. J. Jonas and M. G. Akben), p. 129. Pergamon Press, New York (1985).
36. T. M. Sobolenko and T. S. Teslenko, *High Energy Rate Fabrication IX Int. Conf.*, Academy of Sciences of the USSR, Novosibirsk (1986).